POLITECNICO DI TORINO
Repository ISTITUZIONALE

Optimizing groups of colluding strong attackers in mobile urban communication networks with evolutionary algorithms

(Article begins on next page)

01 September 2025

Wavelet Analysis of a Microbarograph Network

Stefano Grivet-Talocia and Franco Einaudi

Abstract— This paper presents a wavelet-based algorithm for the detection, identification, and extraction of gravity waves from atmospheric pressure traces. The main data processing tool is a nonlinear adaptive filter based on the selective reconstruction of a waveform from its wavelet coefficients. The time-frequency localization of the wavelet transform provides an ideal framework for the decomposition of long-period gravity waves (30 min–6 h), which are characterized by a generally broad spectrum and few oscillation cycles. The procedure is iterative and allows the exhaustive processing of all the events present in a fixed time period.

The waveform of each disturbance is reconstructed with high accuracy. This minimizes the influence of the data-processing technique on the estimate of horizontal speed and direction of propagation, obtained by maximization of the cross-correlation functions between the reconstructed waveforms at the different stations. The introduction of coherency criteria through the network of seven stations allows us to separate the events into two classes. The first includes the events that propagate with very small distortion through the network, while the second includes less coherent but still highly energetic events.

The size of the network and the algorithm developed for the analysis is well suited for the identification and the extraction of those mesoscale disturbances that have a particularly strong influence on the weather as well as on the forecast.

Index Terms— Adaptive filters, adaptive signal processing, data processing, nonlinear filters, pressure measurement, time-frequency analysis, wavelet transforms.

I. INTRODUCTION

THIS PAPER has a twofold objective. First, to present a wavelet transform algorithm for the analysis of pressure data from a network of barographs. Second, to provide preliminary climatological results for the fourth quarter of 1991 on the frequency of occurrence and characteristics of gravity waves detected by such a network.

The motivation for the study stems from the recognition of the important role that gravity waves play in atmospheric dynamics. They redistribute energy and momentum over large distances both horizontally and vertically; they can generate and interact with wind shears and turbulence; they can influence phase changes and thus trigger and generally influence the evolution of convection; and they can couple the troposphere with the layers above, including the ionosphere. Some of these disturbances are essentially confined to the lower few kilometers of the atmosphere, typically with horizontal wavelengths of a few kilometers and horizontal speeds of the order of 10 ms^{-1}, while others involve the entire depth of the troposphere. The latter are characterized by a broad range of horizontal scales and include fronts (500 km), squall lines (100 km), jet-associated vertical wind shears (50 km), and convective cells (5 km). They represent the link between synoptic scale motions and small-scale phenomena. Their speed of propagation ranges from 10 to 100 ms^{-1}, and their amplitude can reach several millibars [3], [28], [40], [49], [51], [52].

The few climatological studies on gravity waves come from networks of pressure sensors (see [13] and [27] and references therein). The pressure at the ground varies in response to changes in the mass of the overlying atmosphere and to vertical accelerations and is, thus, a good indicator of gravity waves. In fact, pressure records are less noisy than temperature or wind or humidity records because they stem from volume integrals. A network of at least three barographs allows the identification of a disturbance horizontal velocity of propagation. We will use in this paper a network of seven barometers, which are located in the vicinity of Flatland, IL.

Each of the atmospheric processes that generate coherent disturbances has its own footprint in the surface pressure. Occasionally, the pressure record is nearly monochromatic, as in the event analyzed in [12], which lasted several periods. The decomposition through fast Fourier transform (FFT) into elementary sinusoids allows a very good analysis of such disturbances. More often, the signal is quite complex and is also localized in time: short wave packets, solitary waves, and sudden pressure changes are such examples. The broad nature of the spectrum for these events makes the data processing techniques based on FFT inappropriate, due to the poor time localization of its basic functions.

The wavelet transform method described in this paper overcomes some of these limitations and allows a good identification of the events in general and of the mesoscale ones in particular. As for the standard FFT, the wavelet transform also allows the decomposition of a signal into a set of basis functions, but these are localized both in time and frequency. This permits a much more efficient detection and reconstruction of an event and minimizes the introduction of spurious correlations.

The wavelet transform is quite new and has been studied and used extensively only in recent years. Many excellent introductory books and papers [4], [7], [23], [42], [45] are available. The range of applications is extremely broad, cov-

ering signal and image processing, data compression, operators theory, information theory, detection, and estimation (see, [6], [39], and [41]). In particular, the detection and extraction of special features of signals, like modulation laws [9], [10], [30] and waves [45], are greatly improved by the wavelet transform.

A number of recent publications show a growing interest in the wavelet transform technique among the geophysical community. Some introductory and review papers have already been published [16], [35], [36]. The wavelet transform has been applied to the study and decomposition of turbulence [1], [5], [26], [29], [31], [32], orthogonal decompositions of spatial rainfall fields [33], [34] and Liquid Water Path (LWP) measurements [22], compression of SAR data [54], disparity analysis [11], quantifications of nonstationarity and intermittency of LWP [8], detection of localized periodicities and climatological fluctuations in Northern hemisphere surface and sea surface temperature (SST) records [36], [38], [44], IR radiance [53], and length of the day (LOD) parameters [20], as well as detection and identification of waves, fronts, and other coherent structures [18], [19], [21], [37], [43], [45], [48]. This paper should be placed in this last category.

An algorithm based on the wavelet transform is presented. It consists of an iterative procedure that identifies the gravity wave events larger than a scale-dependent threshold, extracts their waveforms through a nonlinear adaptive filter, determines relative arrival times at the different stations by maximizing cross-correlation functions, and estimates horizontal speed and direction of propagation with an equivalent plane wave fit. This data-processing technique is ideally suited for the climatological analysis of the data as well as the detailed study of individual events.

Section II provides a brief description of the data and the experimental setup. Section III describes the data processing in detail. The application of this wavelet transform method to the fourth quarter of 1991 is discussed in Section IV. A more detailed analysis for a 45-month period in the 1991–1995 interval is in preparation.

II. DATA DESCRIPTION

This section is devoted to the description of the experimental setup and the data available for the current analysis. Fig. 1 shows the network of seven stations located in the vicinity of the Flatland Observatory near Urbana-Champaign, IL. Each station is equipped with a barograph that measures the surface atmospheric pressure continuously in time with a sampling rate of $T_c = 120$ s and a resolution of the A/D converter of 10 μbars. The time period that was chosen for this analysis is the fourth quarter of 1991, corresponding to a set of seven contemporary time series of 66 240 samples each. Each station has a data gap of about three days, due to malfunctioning of the recording system. In addition, the barometer located at ISW became operative only on day 336 of 1991. Therefore, only six stations are available for part of the analysis.

The geometry of the network, which is characterized by distances between stations ranging 12–45 km, allows a statistical and climatological study of disturbances with characteristic temporal (spatial) scales ranging from several minutes (a
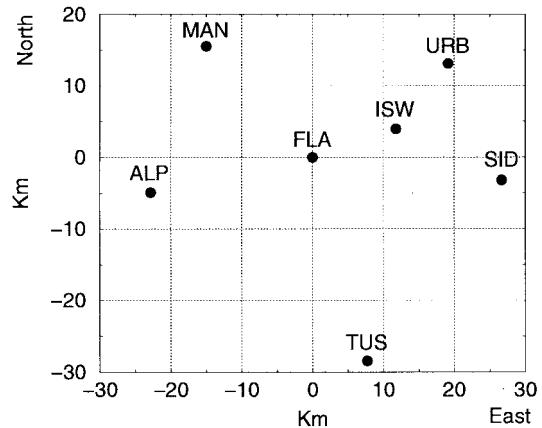

Fig. 1. Geometry of the Flatland barometer network. The coordinate system is centered in the reference station located in Flatland (FLA), IL. The other stations are Allerton Park (ALP), Illinois State Water Survey (ISW), Mansfield (MAN), Sidney (SID), Tuscola (TUS), and Urbana (URB), all located in Illinois.

few kilometers) to several hours (hundreds of kilometers). The present work concentrates on pressure fluctuations with characteristic periods below 6 h. Therefore, a preprocessing highpass filter was implemented to remove longer period fluctuations. The highpass-filtered signals constitute the input raw data set for the main algorithm and will be indicated with the symbols $f_i(t)$ throughout the paper, where the subscript i refers to a specific station. We will denote the reference station (FLA) with the subscript r.

III. DATA PROCESSING

This section is dedicated to a detailed description of the data-processing technique and to the introduction of the algorithm used to extract and study the coherent pressure disturbances propagating through the Flatland barometer network. The filtering procedure is quite complex and is strongly tailored to the application under development. This is due to the extreme variability of the data and especially of the events to be detected. As a matter of fact, every adaptive filtering scheme must be parameterized according to the data being processed. For the sake of clarity, we decided to split the presentation into four sections, each one focusing on a specific aspect of the filter. Section III-A presents a quick overview on the Continuous Wavelet Transform and introduces the nonlinear adaptive filter that allows the selective extraction of gravity wave events from the raw pressure traces. Section III-B is devoted to the derivation of a scale-dependent threshold that provides the main time-frequency localization tool for the filter and to the derivation of the reconstruction region Ω in the wavelet plane for the whole set of stations. Section III-C illustrates the fitting procedure with an equivalent plane wave to detect the most likely speed and direction of propagation associated with the event. The elements discussed in these three sections provide the main building blocks of the iterative extraction algorithm, which is discussed in Section III-D, together with additional consistency tests and classification issues.
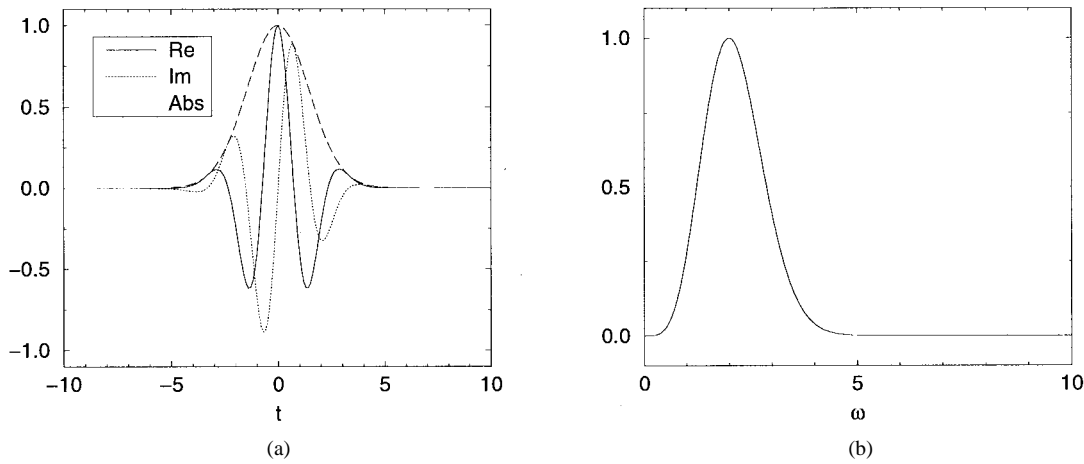
Fig. 2. Basic wavelet: (a) the continuous line represents $\Re\{\psi(t)\}/|\psi(0)|$, the dotted line $\Im\{\psi(t)\}/|\psi(0)|$, and the dashed line $|\psi(t)|/|\psi(0)|$ and (b) the Fourier spectrum $\hat{\psi}(\omega)/\hat{\psi}(\omega_0)$ is plotted, where ω_0 is the centerband angular frequency corresponding to the maximum.

A. Wavelet Transform and Adaptive Filtering

This section contains a short description for the main properties of the wavelet transform and the conventions and symbols used throughout this work. A more complete theoretical background can be found in [4], [7], and [42]. The wavelet transform of a finite energy signal f and its inverse are defined as

$$(Wf)(b, a) = \langle f, \psi_{b,a} \rangle$$
$$= \frac{1}{|a|} \int_{-\infty}^{+\infty} f(t) \psi^* \left(\frac{t - b}{a} \right) dt \tag{1}$$
$$f(t) = C_\psi^{-1} \int_{-\infty}^{+\infty} \int_{-\infty}^{+\infty} (Wf)(b, a) \psi_{b,a}(t) \frac{da\,db}{|a|} \tag{2}$$

where

$$C_\psi = \int_{-\infty}^{+\infty} \frac{|\hat{\psi}(\omega)|^2}{|\omega|} d\omega < \infty. \tag{3}$$

The signal f is decomposed into a set of (nonorthogonal) basis functions $\psi_{b,a}$, derived from a single mother wavelet ψ by means of translations and dilations

$$\psi_{b,a}(t) = \frac{1}{|a|} \psi \left(\frac{t - b}{a} \right). \tag{4}$$

This normalization preserves the L^1 norm when the parameter a, usually called *scale,* is changed. This normalization has been employed in other works [1], [8], [25], [26] and is preferred here because it allows a simple link between the wavelet transform mod and the amplitude of fluctuations in the signal f. More precisely, when analyzing different wave packets with the same amplitude but with different frequency, the wavelet transform mod maxima will be the same. This is not true when the more usual L^2 normalization is used because the wavelet mod maxima would depend also on the frequency. This property will be used in Section III-B.

Several choices for the mother wavelet ψ have been proposed in the literature. The only constraint is the admissibility condition in (3). However, two other requirements are convenient for the analysis and will be imposed here.

The first is the so-called *progressivity.* The basic wavelet ψ is said to be progressive when it belongs to the Hardy space $H^2(\mathbb{R})$, i.e., when its Fourier transform is identically zero for negative frequencies. Such signals, sometimes called *analytical,* are complex valued, and their imaginary part is the Hilbert transform of the real part [46]. In addition, the magnitude can be regarded as the envelope of the real and imaginary part. When a progressive wavelet is used, the reconstruction formula in (2) can be simplified by integrating only the real part over positive scales.

The second issue is a good time-frequency localization. Indeed, the wavelet transform maps a signal into a two-dimensional (2-D) function $W(b, a)$, where the coordinate b corresponds to time and the scale a is inversely proportional to frequency. When equivalent bandwidth and duration of the mother wavelet are finite, the wavelet transform localizes in the space (b, a) the energy of the signal. The bandwidth-duration product has a lower limit dictated by the uncertainty principle [4]

$$\Delta_t \Delta_\omega \geq 1/2. \tag{5}$$

The lower limit is only reached by a Gaussian, which is not admissible as mother wavelet. Several functions ψ with good time-frequency localization properties have been proposed in the literature [24], [45]. The basic wavelet employed in this work is the analytical signal whose real part is the fourth derivative of a Gaussian with variance equal to one. The Fourier transform of ψ is then identically zero for $\omega \leq 0$, while for positive frequencies we have the expression

$$\hat{\psi}(\omega) = 2\sqrt{2\pi}\omega^4 e^{-\omega^2/2}, \qquad \omega > 0. \tag{6}$$

It can be shown that $\psi(t)$ is proportional to $e^{-t^2/4} D_{-5}(-jt)$, where D is one of the parabolic cylinder functions [15]. The real and imaginary parts as well as the mod of $\psi(t)$ are plotted in Fig. 2(a) and its Fourier spectrum in Fig. 2(b). The mod decays in time as $|t|^{-5}$. The relative band is $\Delta_\omega/\omega_0 \simeq 0.24$ and the bandwidth-duration product is $\Delta_t \Delta_\omega \simeq 0.51$. These properties insure a good time-frequency localization. The normalization constant for the inversion formula is $C_\psi = 24\pi$.
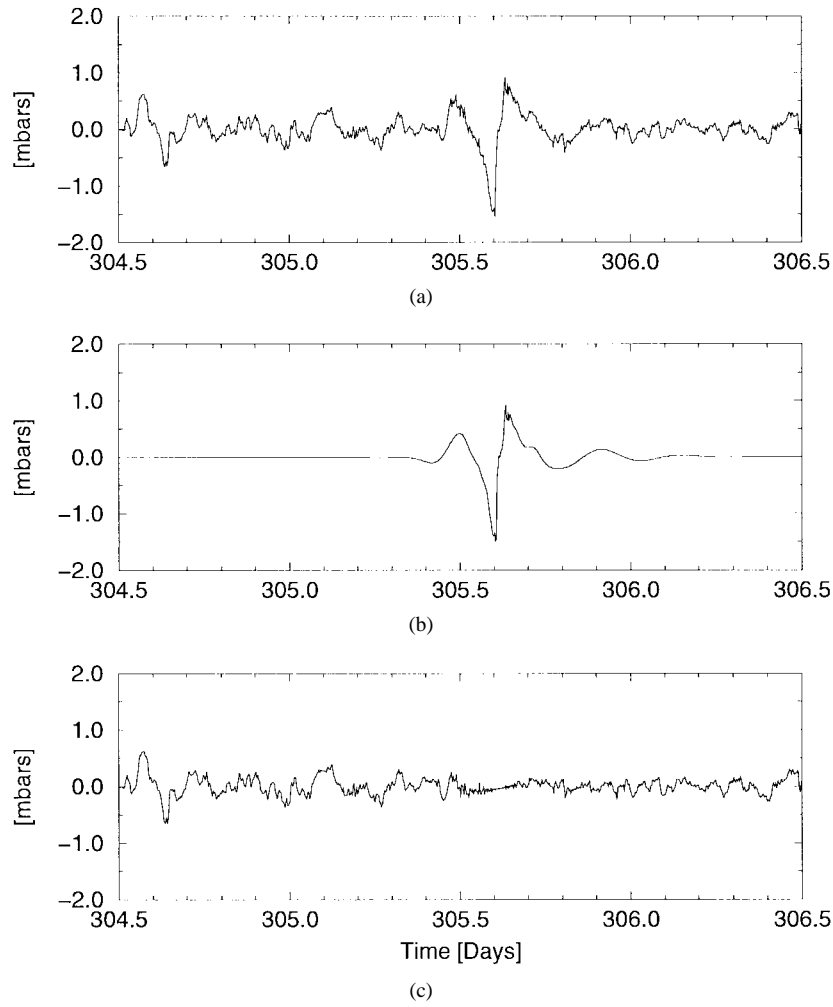
Fig. 3.   Event extraction. (a) Original pressure series, (b) extracted event, and (c) remaining waveform after the extraction.

It should be noted that the time localization of this wavelet is more strict than the frequency localization. This property is essential for an efficient filtering of waveforms, like solitary waves, bumps, or sudden jumps, that are intrinsically of broadband nature and very localized in time. The employment of other wavelets, like the Morlet wavelet, with better frequency resolution would not lead to satisfactory results, especially in the separation of close disturbances (see Section III-B). Any choice of wavelet that is admissible, progressive, and has these time-frequency localization properties could be used here.

Due to the exact reconstruction formulas, the operations of taking the wavelet transform and its successive inversion can be interpreted as the application of the identity operator in the space of real signals with finite energy. This is achieved when the integration is performed in (2) over the whole plane (or halfplane) Σ. It is possible to define a class of bounded operators by restricting the integration domain to a smaller region $\Omega \subset \Sigma$. These operators have many interesting properties [7]. When Ω is determined *a priori* and does not depend on the signal itself, the resulting operator is linear. Nonetheless, very powerful filters can be constructed by adapting the reconstruction region to the signal being processed, setting $\Omega = \Omega(f)$. The resulting operator will then be nonlinear. The raw signal f can thus be adaptively separated

into two components

$$p(t) = 2C_\psi^{-1} \iint_{\Omega(f)} \Re\{\langle f, \psi_{b,a}\rangle \psi_{b,a}\} \frac{da\,db}{a} \qquad (7)$$

$$f(t) - p(t) = 2C_\psi^{-1} \iint_{\Sigma - \Omega(f)} \Re\{\langle f, \psi_{b,a}\rangle \psi_{b,a}\} \frac{da\,db}{a}. \qquad (8)$$

The actual filter for the extraction of gravity wave events operates on multivariate signals to process the pressure traces in all the stations at the same time. Therefore, the determination of Ω is based on the combined extraction of the event from all stations and will be discussed in Section III-B. We will now illustrate the effectiveness of the filter in (7) on a single pressure signal. A two-day data segment centered in day 305 of year 1991 is shown in Fig. 3(a). This is the original pressure track recorded at the reference station (Flatland) after the preprocessing highpass filtering that eliminates the long-period fluctuations. The signal includes then all the fluctuations in the range of periods between four minutes (corresponding to the Nyquist frequency) and six hours. A well-defined disturbance is evident from the plot.

The mod of the wavelet transform $|(Wf)(b, a)|$ is reported in Fig. 4(a). The horizontal axis corresponds to time b and the vertical axis, which is logarithmically spaced, to frequency $\omega_0/2\pi a$. An analysis of this plot allows a qualitative identifi-
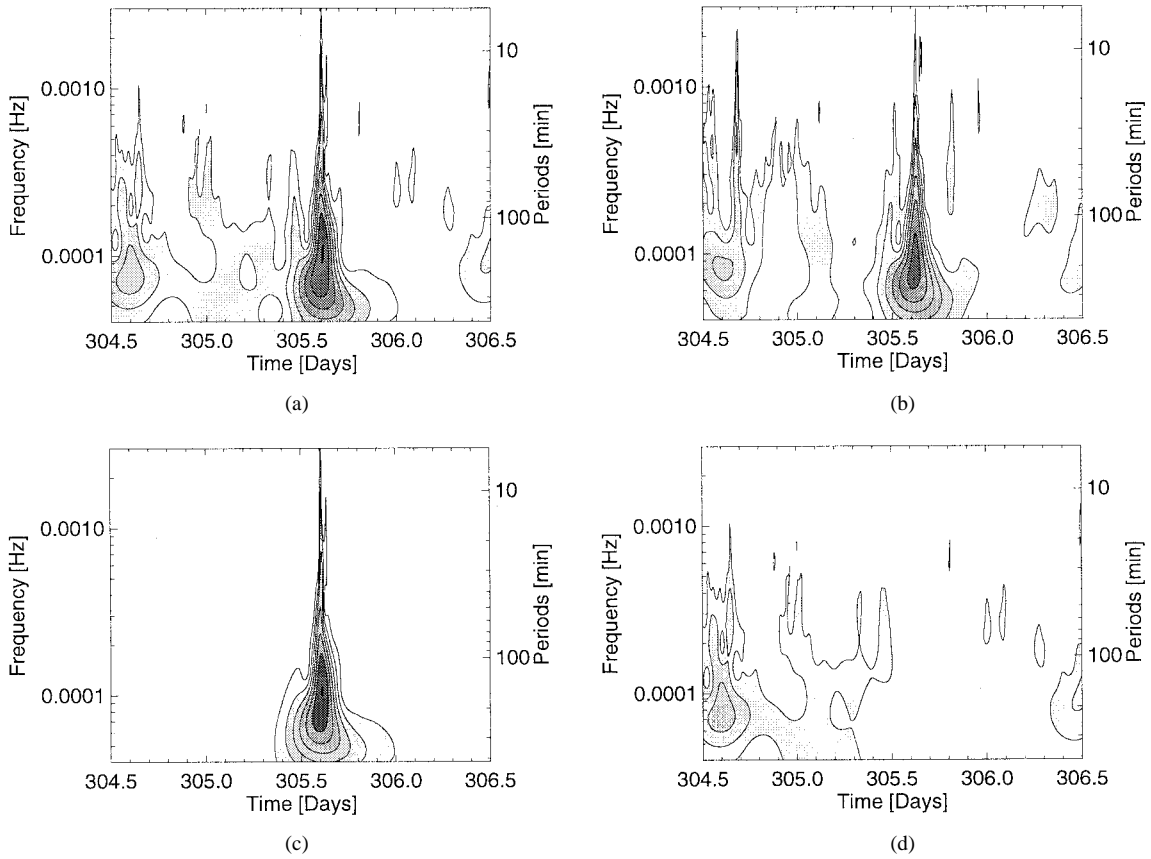
Fig. 4.   Wavelet transform (magnitude) shown as a contour plot for (a) raw signal f_r [Fig. 3(a)], (b) raw signal f_i at a different station (URB), (c) extracted event p_r [Fig. 3(b)], and (d) remaining signal $f_r - p_r$ [Fig. 3(c)]. The intensity of the gray shades is proportional to the magnitude of the wavelet transform.

cation of a subset of points in the time-scale plane with large wavelet amplitude (darker region). Taking this region as $\Omega(f)$ and applying (7), we obtain the signal plotted in Fig. 3(b). Its wavelet transform is given in Fig. 4(c) and illustrates the set of retained time-frequency components in the filtered signal $p(t)$. Also, the remaining part $f(t) - p(t)$ is plotted in Fig. 3(c) and its wavelet transform in Fig. 4(d). It is clear from these plots that the filter is capable of extracting the wave from the background fluctuations with very high selectivity.

B. Definition of the Reconstruction Region Ω

In Section III-A, we showed that there is a one-to-one correspondence between what we define an event and a region in the time-scale plane with significantly high and localized wavelet amplitude. It is crucial to define an algorithm that automatically finds an event and determines the optimal reconstruction region Ω .

Let us consider first a single pressure trace. Once an event has been identified in the plane (b, a), the reconstruction region could be found by retaining only those points with wavelet coefficients larger than a fixed threshold. However, power spectra of various geophysical quantities, including the pressure [2], have been shown to have a characteristic power-law decay in frequency. This means that the amplitude of a disturbance could be considered insignificant at long periods, but quite significant at short periods. It seems thus appropriate to use a scale-dependent threshold.

The threshold that will be used in the following is the time-averaged wavelet amplitude, which provides a scale-dependent amplitude spectrum for the overall time series. It is defined as

$$A(a) = \frac{2}{\hat{\psi}_0} \langle |(Wf)(b, a)| \rangle_b \qquad (9)$$

where the normalization constant $\hat{\psi}_0 = \hat{\psi}(w_0)$ insures that the amplitude $A(a)$ is equal to the amplitude of a monochromatic wave at the frequency corresponding to the scale a [25]. The function $A(a)$ has been evaluated over the available data set (three months), averaging over all the stations of the network, and is plotted in Fig. 5 (continuous line), where the horizontal scale axis is labeled with periods $T = 2\pi a/\omega_0$.

The location of an event is determined by maximizing the function

$$\max_{b,a} \frac{|(Wf)(b, a)|}{A(a)}. \qquad (10)$$

Once this "center" (b_c, a_c) has been found, the set of points Ω' with wavelet amplitude above the threshold is defined by

$$(b_c, a_c) \in \Omega' \qquad (11)$$

$$(b, a) \in \Omega' \Leftrightarrow |(Wf)(b, a)| \geq A(a) \qquad (12)$$

$$\Omega' \text{ is connected.} \qquad (13)$$

The reconstruction region Ω is obtained by extending Ω' along the a and b directions until the first minimum of $|(Wf)(b, a)|$ is found. This correction is needed to improve the waveform
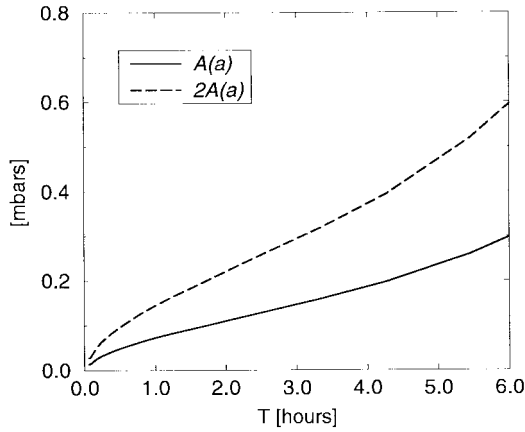
Fig. 5. Scale-dependent thresholds. The time-averaged wavelet amplitude $A(a)$ is plotted versus periods (continuous line). The quantity $2A(a)$ is also drawn (dashed line).

reconstruction because, although the wavelet transform in $\Omega - \Omega'$ is below the threshold, its contribution to the energy of the event can be substantial, since Ω can be much larger than Ω'. The localization, though, is not affected by this process because only the time-scale components pertaining to the event under investigation are included in its reconstruction region. This algorithm was used in the example of Section III-A (Fig. 4).

It should be noted that an event can be extracted only if

$$|(Wf)(b_c, a_c)| \geq A(a_c) \qquad (14)$$

otherwise, the reconstruction region Ω would be an empty set. A faithful and stable reconstruction, however, requires a more stringent condition. Indeed, when $|(Wf)(b_c, a_c)|$ is larger but almost equal to $A(a_c)$, there are few and possibly only one point of the discrete grid in the auxiliary set Ω' and the final reconstruction region Ω will be correspondingly small. This means that the reconstructed signal will be a superposition of too few basis functions, its waveform p_i will have little resemblance with the corresponding disturbance in the raw signal f_i, and the event should be disregarded. This situation can be avoided by requiring

$$|(Wf)(b_c, a_c)| \geq \alpha_M A(a_c) \qquad (15)$$

where α_M is a multiplicative factor sufficiently larger than one, and yet not too big to avoid missing a significant event. After extensive testing, we chose $\alpha_M = 2$. This more restrictive threshold is plotted in Fig. 5 (dashed line).

It proved also useful to introduce an additional parameter α to control the selectivity of the reconstruction. The new threshold $\alpha A(a)$ was considered and substituted into (12), obtaining

$$(b, a) \in \Omega'_\alpha \Leftrightarrow |(Wf)(b, a)| \geq \alpha A(a). \qquad (16)$$

The set Ω'_α is now dependent on α. As α increases, the localization is more strict and Ω'_α is smaller. When α decreases, more points are included and the localization is less selective. This selectivity parameter can be varied in a range $[\alpha_{\min}, \alpha_{\max}]$. The lower bound is taken as $\alpha_{\min} = 1$ to insure that the time-frequency components of the event are

above average fluctuations. The upper bound must insure both a sufficiently small threshold, with respect to the magnitude of the event, and the inclusion of most of its energy. This requirement can be accomplished by setting

$$\alpha_{\max} = \min\left\{\alpha_M, \frac{|(Wf)(b_c, a_c)|}{\alpha_M A(a_c)}\right\}. \qquad (17)$$

The procedure for the determination of the optimal value of α will be described in Section III-D.

Let us turn now to the whole set of stations $\{S_i, \ i = 1, \cdots, N_s\}$, with $S_1 = S_r$ denoting the reference station. Suppose that a well-defined event has been identified and reconstructed at S_r by using the procedure described above. The next step is the identification and extraction of the waveform corresponding to the same event in stations $S_i, \ i > 1$. This operation is generally not simple for two main reasons. First, it is not known when the event occurs in time. The relative time difference between the arrival times at stations S_i and S_r depends on speed and direction, which are the parameters to be estimated by the whole procedure. There are physical lower and upper bounds for the propagation speed, which can be easily translated into bounds for the delay times, because the distance between the stations is known. However, there is a need for an automatic search of the arrival time in each station S_i. Even more important, there must be no ambiguity. When two different events are very close in time, the algorithm must insure the detection of the same event in all stations. Second, the waveform of the event is generally not invariant during its propagation. A number of reasons, including instability effects and local fluctuations, contribute to modifying the pressure disturbance in time and space. This means that the reconstruction region changes shape at the different stations. On the other hand, the waveform distortions for a well-defined event must be small, otherwise the hypothesis of the existence of a propagating disturbance ceases to be valid. Likewise, the changes in Ω_i from station to station must be small. As an example, the wavelet transform of the raw pressure track at another station (URB) corresponding to the event examined in Section III-A is plotted in Fig. 4(b). Note the global similarity and the differences in the details with Fig. 4(a). In this particular case, the event was propagating quite coherently through the network (see below), and therefore, the differences in the reconstruction regions at the different stations were small. However, the question of whether the event is coherent (i.e., the distortions are small and the propagation speed is well defined) can only be answered on a statistical basis. The complete set of criteria employed by the extraction algorithm will be itemized in Section III-D.

Let Ω_r be the reconstruction region in the reference station. We introduce a time-shifted set in the time-scale plane

$$\Omega_{rs}(s) = \{(b + s, a)|\ (b, a) \in \Omega_r\} \qquad (18)$$

which is an exact copy of Ω_r translated in time by s. If the distortions between the stations are not too large, the true reconstruction region Ω_i in S_i will not be very different from
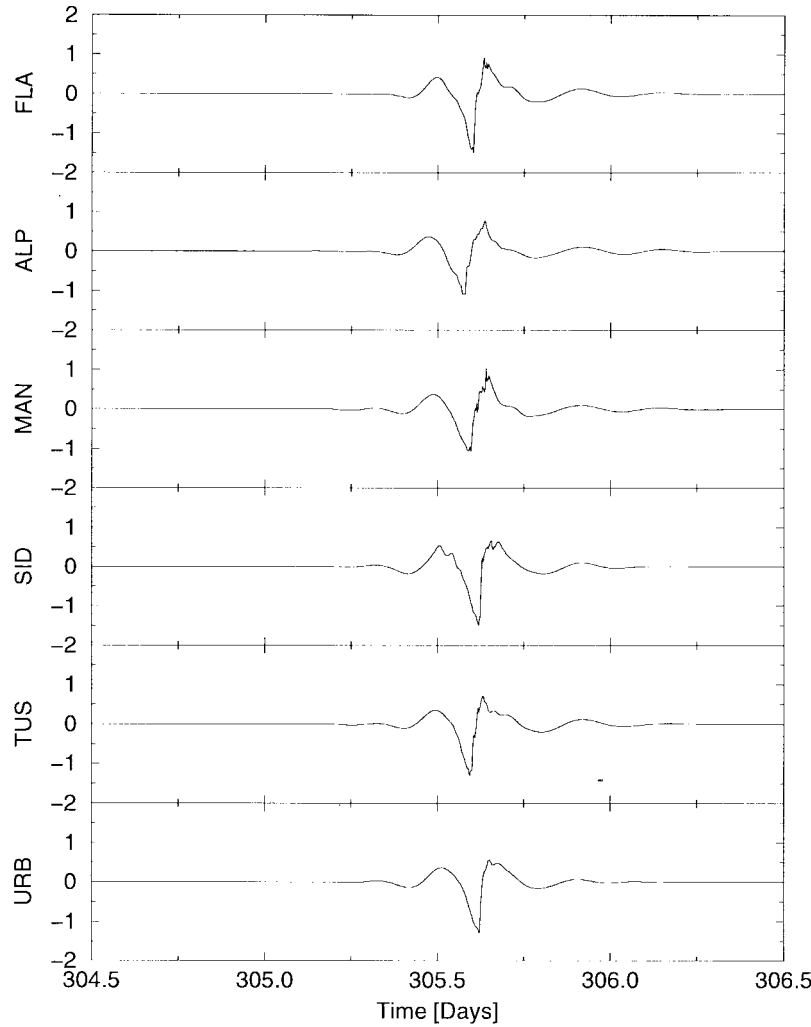
Fig. 6.　Extracted event p_i for the available stations. The vertical axis corresponds to pressure fluctuations [mbars].

$\Omega_{rs}(s_{ri})$, where s_{ri} is the propagation delay time between the stations. Moreover, if the raw signals corresponding to the events are similar, so will be their wavelet transforms. The optimal delay time s_{ri} can then be found maximizing a cross-correlation function between the two wavelet transforms at the two stations. This function is defined as

$$G_i(s) = \iint_{\Omega_r} \Re\{(Wf_r)(b, a)\}\Re\{(Wf_i)(b+s, a)\} \frac{da\,db}{a}.$$

(19)

The optimal delay time s_{ri} is such that $G_i(s_{ri}) > G_i(s) \,\forall\, s \neq s_{ri}$. Once s_{ri} has been found, a first estimate of the reconstruction region for station S_i is given by $\Omega_{rs}(s_{ri})$. However, this first estimate must be refined. This refinement is performed by finding the center (b_{ci}, a_{ci}) that maximizes the wavelet amplitude in the set $\Omega_{rs}(s_{ri})$ and then by applying again the algorithm described above.

Repeating the above steps for $i = 2, \cdots, N_s$, we obtain a set of reconstructed waveforms for a specific event for all the stations. These signals, hereafter denoted with $p_i(t)$ are identically zero everywhere except in the support of the disturbance. The resulting waveforms at the available stations

for the same event studied in the previous section are plotted in Fig. 6.

It has already been mentioned that particular care must be taken in the extraction of a single event from a network since local and propagation effects can create anomalies in some of the stations. Examples of such anomalies follow.

• When two or more separate disturbances are close in time, their reconstruction regions may overlap. Intuitively, if we regard the wavelet magnitude as a three-dimensional (3-D) surface, the events are like "mountains" separated by "valleys". When a valley is completely below the threshold $A(a)$, the events have distinct reconstruction regions and can be separated easily. On the other hand, when two events are very close and propagate with significantly different velocities, their time separation varies from station to station. This means that the distance between the peaks of the two mountains in the wavelet plane changes and the separating minima can be above the threshold for some stations and below for others. This leads to the two events being identified as separate at some stations and as single at others. The question regarding whether the two events have to be separated can only be answered on a statistical basis.
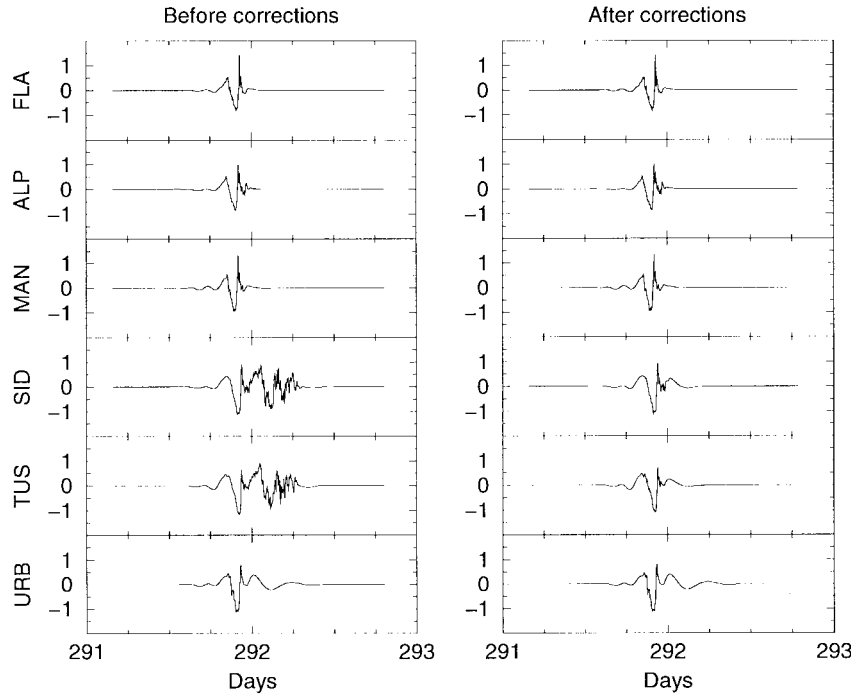
Fig. 7.   Example of an event that was improved by the corrections described in Section III-B. The reconstruction was consistent in all stations except for SID and TUS. The right column shows the reconstructed waveforms after the corrections. The pressure units are [mbars].

- Local phenomena, like a thunderstorm occurring in the vicinity of one station, can interact with a well-defined event that propagates through the network and modify its waveform. The time-frequency signature of the event is then distorted.
- A well-defined event may be characterized by a spatial domain that does not include all the stations of the network. In this case, the pressure signal in some of the stations does not allow the identification of any reconstruction region for the event.

A set of statistical tests has been designed to determine if the reconstruction regions Ω_i are consistent throughout the network in either shape or position. The shape can be analyzed by restricting the reconstruction regions to constant-a lines (usually called *voices*), therefore obtaining intervals $[b_i'(a), b_i''(a)]$. The shapes are consistent throughout the network when the widths $\delta_i(a) = b_i''(a) - b_i'(a)$ follow a narrow distribution around a certain mean value for each voice. When one considers the same set minus one station, the distribution will not be very different. On the other hand, when there is one station with significantly different reconstruction region and consequently significantly different $\delta_i(a)$, this distribution will change dramatically when this station is subtracted from the set. In particular, the variance will be large when considering all the stations and will drop when neglecting the "bad" station. Note that this is true when the bad station has either larger or smaller reconstruction region. When one of the "good" stations is neglected, however, the variance will remain large. The presence of a station with a significantly different Ω_i can be determined through the application of the standard F-test [47] to the distribution of the $\delta_i(a)$'s. The case when the center (b_{ci}, a_{ci}) has been misidentified

is detected similarly by analyzing the distribution of the b_{ci}'s. This leads, when necessary, to the correction of the defective Ω_i's. For each fixed scale we redefine the boundary points of the reconstruction region as

$$b_i'(a) = \frac{1}{N_s - 1} \sum_{j \neq i} b_j'(a) - s_m \qquad (20)$$

$$b_i''(a) = \frac{1}{N_s - 1} \sum_{j \neq i} b_j''(a) + s_m \qquad (21)$$

where s_m is the maximum propagation delay evaluated among the valid stations

$$s_m = \max_i \{|s_{ri}|\}. \qquad (22)$$

These equations place the reconstruction region as close as possible to where the event is expected on the basis of the data from the other valid stations. Moreover, its shape is dependent on the Ω_i's in the good stations. It should be noted that the tests mentioned above will also work when the bad stations are two, in which case we have similar expressions. The need for the above corrections is exemplified in Fig. 7. Two close events occurring in days 291 and 292 were incorrectly merged into the same waveform in stations SID and TUS and successfully corrected. These tests cannot be used to detect more than two bad stations because they would lose statistical significance.

C. Speed and Direction Estimation

This section will describe the procedure adopted for the estimation of propagation speed and direction, once the waveforms of a given event in all the stations have been extracted. The first step is the determination of the arrival time t_i at each
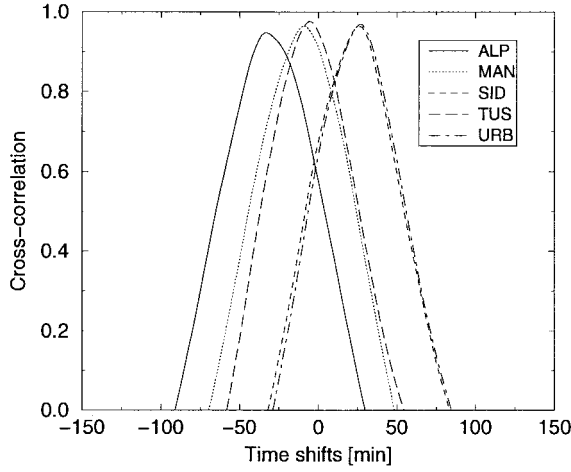
Fig. 8. Cross-correlation functions between the reconstructed waveform at the stations S_i and S_r for the event reported in Fig. 6.

station S_i relative to the arrival time t_r at the reference station

$$\Delta t_i = t_i - t_r, \qquad i = 2, \cdots, N_s. \tag{23}$$

These delays can be easily calculated by maximizing the standard cross-correlation functions

$$C_i(\tau) = \frac{1}{\|p_r\| \, \|p_i\|} \int p_r(t) p_i(t + \tau) \, dt. \tag{24}$$

Note that these cross-correlation coefficients are evaluated on the cleaned waveforms p_i of the events and not on the raw time series f_i. This is one of the main advantages of the wavelet-filtering procedure because fluctuations that are extraneous to the event have minimal influence on the delay times. This fact insures very high cross-correlation coefficients. An additional advantage of this filtering technique is that there is no ambiguity in the determination of the integration domain in (24) because the extracted waveforms are localized in time. The cross-correlation functions for the event reported in Fig. 6 are plotted for all stations in Fig. 8. The relative delay times Δt_i are such that

$$C_i(\Delta t_i) > C_i(\tau), \qquad \forall \, \tau \neq \Delta t_i. \tag{25}$$

Let us consider now the estimation of speed and direction from the set of delay times. The basic hypothesis underlying the analysis is that each event is characterized by well-defined propagation speed and direction, which are constant through the network. In other terms, each event can be represented by an equivalent plane wave. If this hypothesis is not satisfied, as in the case of two or more propagating wave packets with different velocities, the algorithm will evaluate a mean speed and direction and is likely to reject the event on the basis of the tests described in Section III-D. The model for the disturbance is

$$p_i(t) = p(t - \mathbf{s_w} \cdot \mathbf{r_i}) \tag{26}$$

where $\mathbf{s_w}$ is the slowness vector [14] and $\mathbf{r_i}$ is the relative position of the station S_i, with respect to the reference station. It should be noted that the slowness vector points toward the direction of propagation of the event ϑ_w, and its magnitude

is the inverse of the phase speed $s_w = 1/v$. The convention for the propagation directions assumes angles measured east of north. The calculation of the theoretical arrival times of the model in the station i is straightforward and leads to

$$\Delta t_i^m = s_w r_i \cos(\vartheta_i - \vartheta_w) \tag{27}$$

where ϑ_i is the angular coordinate of the station. The best-fitting slowness vector is found by a standard χ^2 minimization

$$\chi^2(s_w, \vartheta_w) = \frac{1}{T_c^2} \sum_{i=2}^{N_s} (\Delta t_i^m - \Delta t_i)^2 \tag{28}$$

where the normalization constant is the sampling time and makes the χ^2 statistic nondimensional. Note that the discrepancies between the measured and theoretical delay times are due to many factors and, in general, cannot be assumed to be Gaussian. Therefore, the standard Q statistic [47] cannot be used for producing a level of significance of the fitting. The quantity that will be used is

$$\delta t_{\text{rms}} = \sqrt{\frac{1}{N_s - 1} \chi^2} \tag{29}$$

and indicates the rms deviation of the measured delay times from the model delay times normalized with the sampling time. It will be denoted in the following with fitting error.

D. Global Iterative Events Extraction

A climatological study on pressure disturbances requires the systematic identification of all significant events from the data stream. The algorithm introduced in the preceding sections can be applied iteratively on the highpass-filtered pressure time series to extract the events one by one. This procedure is summarized as follows.

1) Evaluate the wavelet transform of the pressure signals for all the stations in the whole time period under analysis.
2) Find the event with the largest amplitude.
3) Extract the event, find the delay times between the stations, and fit the equivalent plane-wave propagating model.
4) Evaluate the remaining signals after the extraction at all stations and recompute their wavelet transform.
5) Repeat Steps 2)–4) until a loop-breaking condition is reached.

Steps 1) and 4) are direct numerical implementations of (1) and (8) and do not need additional explanations. Steps 2) and 5) have already been discussed in Section III-B and are expressed, respectively, by (10) and (15). Step 3) combines the procedure described in the preceding sections with a classification algorithm. This classification is important because it must allow the detection of truly coherent events from other phenomena. There are basically three classes of events that can be encountered.

1) Events with high cross-correlation coefficients and good fitting. These events correspond to well-identified localized disturbances that propagate through the network, and their speed and direction can be evaluated with a

good confidence level. These will be labeled as "class 1 events".

2) Events with sufficiently large amplitude and good wavelet reconstruction, but either with low cross-correlation coefficients or bad fitting. These disturbances correspond to localized perturbations not coherent through the stations, or with a dominant frequency (wavelength) not suitable to the geometry of the network. They will be named "class 2 events" in the following and will be further discussed in Section IV-C.

3) Events with small amplitude, poor correlation coefficients, and bad fitting. These are disregarded in the statistics, but must be subtracted from the pressure traces so that the algorithm can proceed to the next iteration.

The classification algorithm is embedded in the decision procedure that selects the optimal value of the selectivity parameter α and determines the reconstruction regions Ω_i's and the extracted waveforms $p_i(t)$. The first attempt of a reconstruction is made for the upper bound $\alpha = \alpha_{\max}$. Events that are well defined and stable throughout the network have a strong signature in the time-scale plane at all stations and are immediately reconstructed with high accuracy. When the reconstruction is detected as bad, even after the corrections described in Section III-B, α is lowered and another attempt is made. This procedure is repeated until $\alpha_{\min} = 1$ is reached or the event is identified in the class 1. Lower values of α allow a more flexible reconstruction in the different stations for events characterized by more distorted waveforms. Before being placed in class 1, each event must also satisfy additional stringent conditions on the correlation coefficients $K_i = C_i(\Delta t_i)$ and on the fitting error. These conditions are itemized below.

- The correlation coefficients must be sufficiently high and the fitting error sufficiently small. We found that all the events with a strong signature always satisfy the condition

$$K_{\min} \geq 2/3 \quad \text{and} \quad \delta t_{\mathrm{rms}} \leq 2 \tag{30}$$

where $K_{\min}$ is the minimum cross-correlation coefficient. When these conditions are not satisfied, a further F-test on the set of cross-correlation coefficients $\{K_i\}$ is attempted to detect whether one or two stations have poor correlations with respect to the others. Eventual corrections are applied to the bad stations. If (30) is still not satisfied, some looser conditions are then tested, allowing either worse correlations or a larger fitting error

$$\overline{K} \geq 0.75 \quad \text{and} \quad \delta t_{\mathrm{rms}} \leq 0.5 \tag{31}$$
$$\overline{K} \geq 0.8 \quad \text{and} \quad \delta t_{\mathrm{rms}} \leq 3 \tag{32}$$

where $\overline{K}$ is the mean cross-correlation coefficient. When both of these conditions are still not satisfied, a last attempt is made on a restricted set of stations, neglecting the one with the lowest correlation coefficient. If this attempt succeeds, the event is placed in the class 1 and is interpreted as a localized disturbance that does not propagate coherently throughout the whole network, but only on a subset of stations.

- The fitting error δt_{rms} must be small, with respect to the propagation time through the network, otherwise the uncertainty on the fitted speed and direction would be too large. A test that was found by trial and error to be appropriate is given by

$$\delta t_{\mathrm{rms}} \leq 0.4 \Delta t_{\mathrm{rms}} \tag{33}$$

where Δt_{rms} indicates the rms propagation delay time through the network normalized with the sampling time

$$\Delta t_{\mathrm{rms}} = \frac{1}{T_c} \sqrt{\frac{1}{N_s - 1} \sum_{i=2}^{N_s} (\Delta t_i^m)^2}. \tag{34}$$

- The speed must be confined within physical bounds. When Δt_{rms} is too small, the estimated speed would be too large and would not have any physical meaning. This is the typical situation of some small high-frequency fluctuations belonging to the waveform of an event already extracted that were left over in its reconstruction. The implemented test was

$$\Delta t_{\mathrm{rms}} \geq 2 \tag{35}$$

which means that the rms propagation time must be at least twice the sampling time T_c.

- Only events characterized by a ratio between the second and the first positive maximum of the cross-correlation functions less than 0.8 were accepted. This latter test allows to reject high-frequency events suffering from spatial aliasing.

IV. NUMERICAL RESULTS

A. Complete Events Extraction from Pressure Records

The iterative algorithm described in Section III was applied to the pressure data from the Flatland barometer network. Only a three-month period corresponding to the fourth quarter of 1991 is processed in this paper to illustrate the data-processing technique. A longer pressure record will be analyzed in a forthcoming paper.

The remaining signals after the extraction of all the events are

$$e_i(t) = f_i(t) - \sum_{k=1}^{N_t} p_i^{(k)}(t) \tag{36}$$

where N_t is the total number of iterations and $p_i^{(k)}$ is the extracted waveform of the event k in station S_i. The signals f_r and e_r at the reference station and the time supports of class 1 and 2 events are plotted in Fig. 9(a)–(d) for three weeks in the period under investigation. The comparison of $f_r(t)$ and $e_r(t)$ clearly illustrates the power of the described method in the selective extraction of events.

The total number of identified events was $N_e = 138$, of which only $N_g = 56$ were placed in class 1. The remaining $N_b = 82$ (class 2) events had significant amplitude, with respect to the scale-dependent threshold $A(a)$, but no fitting was possible. A further discussion of these events will be given in
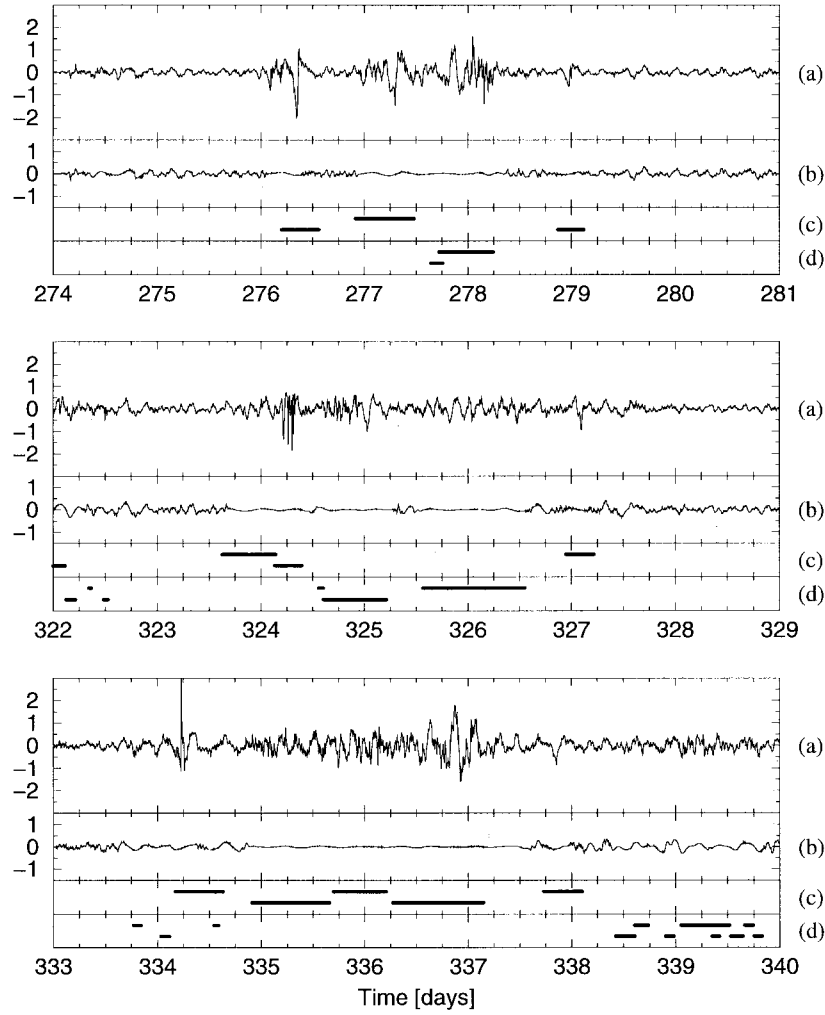
Fig. 9. (a) Raw highpass-filtered signals f_r and (b) remaining signals e_r after the extraction of all events at the reference station for three weeks in the fourth quarter of 1991. The supports of class 1 and 2 events are shown, respectively, in (c) and (d). The pressure fluctuations units are [mbars].

Section IV-C. In addition, other $N_0 = 428$ small fluctuations were extracted, but with amplitude smaller than the threshold. These were mainly due to noncomplete reconstructions of previous events or to high-frequency glitches in the pressure record. They had to be extracted to clean the original waveform and allow the algorithm to jump to the next iteration, but were not considered in any of the statistics illustrated in this paper. In conclusion, a total of $N_t = N_e + N_0 = 566$ iterations were necessary before reaching the loop-breaking condition in (15).

As already discussed in Section III, the algorithm extracts the pressure disturbances one by one. It is possible then to evaluate the amount of extracted energy for each iteration. In particular, the following quantity was evaluated:

$$E(k) = \|f_r\|^{-2} \left\| f_r - \sum_{j=1}^{k} p_r^{(j)} \right\|^2 \qquad (37)$$

which is the normalized energy in the signal after the first k iterations. This quantity is plotted in Fig. 10(a), where the sum includes all N_e events (dashed line) and only class 1 events (continuous line). Note that about 46% of the initial energy belongs to class 1 events, while the extracted energy

of the total events reaches 65%. The energy decay in the first 20 iterations is particularly fast. This is because the first events to be identified happen to have large amplitude and low frequency.

Similarly to $E(k)$, the frequency of occurrence $\zeta(k)$, defined as the percentage of time when events are present with respect to the total time, was evaluated and plotted in Fig. 10(b) as a function of k. The two different cumulative time percentages refer to all events together (dashed line) and to class 1 events only (continuous line). Only the asymptotic values of these plots are of physical significance. However, from the steep slope of these curves in the extraction of the first events, we can conclude that the most energetic events, which are immediately extracted by the algorithm, are also characterized by a long duration. After the algorithm stops and all events are extracted, the class 1 events cover approximately 18% of the total time, while all events together cover 31%.

After each event is extracted, it can be further processed to estimate its equivalent frequency band, defined as the frequency interval including most of its energy. Fig. 11 reports a histogram of the number of class 1 and 2 events in different periods bins. The thick line represents class 1 events, and the
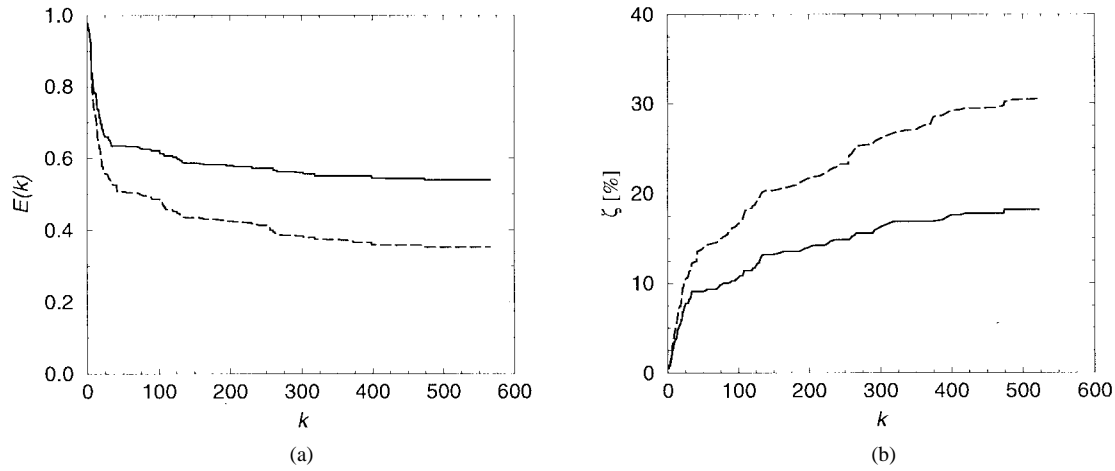
Fig. 10. (a) Energy $E(k)$ of the signal remaining after the first k iterations, normalized with the total initial energy of the raw highpass-filtered signal, as indicated in (37). The continuous line takes into account only the extracted class 1 events, and the dashed line includes all events. (b) Frequency of occurrence $\zeta(k)$ for class 1 events (continuous line) and class 2 events (dashed line).
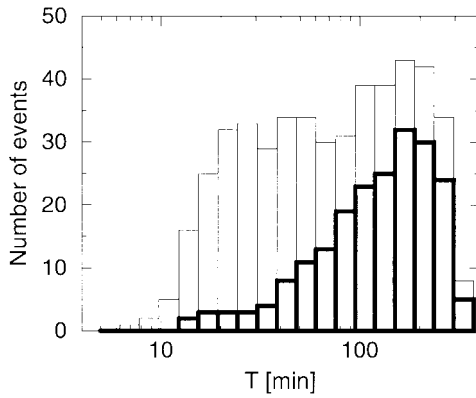

Fig. 11. Distribution of class 1 (thick line) and all (thin line) events in periods bins. Both histograms start from zero, and the difference corresponds to class 2 events. The plot refers to the fourth quarter of 1991.

thin line all events. It should be noted that the consideration of all events leads to an almost uniform distribution of periods, while the class 1 events are concentrated in the longer periods range. The cutoff period can be estimated from the plot to be $\hat{T} = 20 - 30$ min. Speed and direction for higher frequency events cannot be estimated uniquely by this network and will require a set of stations with smaller separations.

B. Class 1 Events

This section presents the results relative to the class 1 events characterized by high cross-correlation coefficients between the stations, low error in the fitting with an equivalent plane wave, and significant amplitude [compared to the scale-dependent threshold $A(a)$ introduced in Section III-B]. Typical amplitude values range from 0.2 mbars at 10 min to several millibars at 2 h. The delay times Δt_i in the different stations are known, so the mean waveform for event j can be found by averaging the time-shifted waveforms in the different stations

$$\overline{p}_j(t) = \frac{1}{N_s} \sum_{i=1}^{N_s} p_i^{(j)}(t + \Delta t_i) \qquad (38)$$

where the delay time in the reference station is assumed $\Delta t_r = 0$. A plot of the averaged waveforms for all the class 1 events occurring in the three weeks shown in Fig. 9 is given in Fig. 12.

The basic parameters evaluated for each event, speed v and direction ϑ_w, are plotted in Fig. 13. The error bars have been produced by fitting the equivalent plane wave model to subsets of three stations, including Flatlands and defining nonoverlapping regions, and taking the minimum and maximum fitted parameters. All the speeds are in the range 9–47 ms^{-1}, with the largest contributions between 20 and 40 ms^{-1}. The directions of propagation have a positive component pointing toward east, and most of them are concentrated in the sector between NE and SE.

C. Class 2 Events

The set of class 2 events is composed of sufficiently large amplitude disturbances for which no fitting was possible. These events are considered to be present, but their propagation speed and direction cannot be found. There are different reasons for the failure of the fitting procedure, resulting in a further classification. There are mainly three categories.

i) Some pressure fluctuations are not coherent at all stations and suffer from local variations. The resulting cross-correlation coefficients are then quite small and the estimates of the arrival times cannot be trusted. An example is shown in Fig. 14 for the available stations (six in this case). It should be noted that the waveform is well defined in all stations, but the distortions are too large for a good estimate of the delay times using the cross-correlation functions. A possible reason is the presence of two interacting wave packets with a different propagation speed and direction, which cannot be separated because their time-frequency components are overlapping in the wavelet plane and interfering with each other.

ii) Some events are resulting from a nonperfect reconstruction of other larger events already processed by the algorithm. Even when small, with respect to the
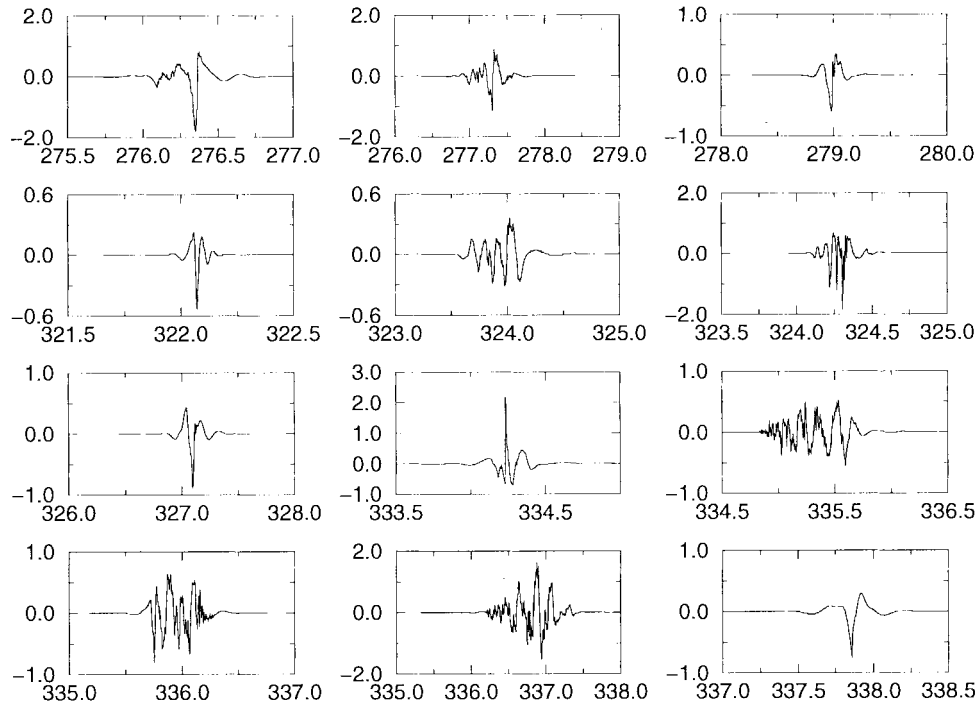
Fig. 12. Averaged waveforms of the class 1 events occurring in the periods shown in Fig. 9. The events are plotted in chronological order from left to right and from top to bottom. The pressure fluctuation units are [mbars], and the time units are days [UTC]. Note that the scales for the time and pressure axes are not the same in the different panels.
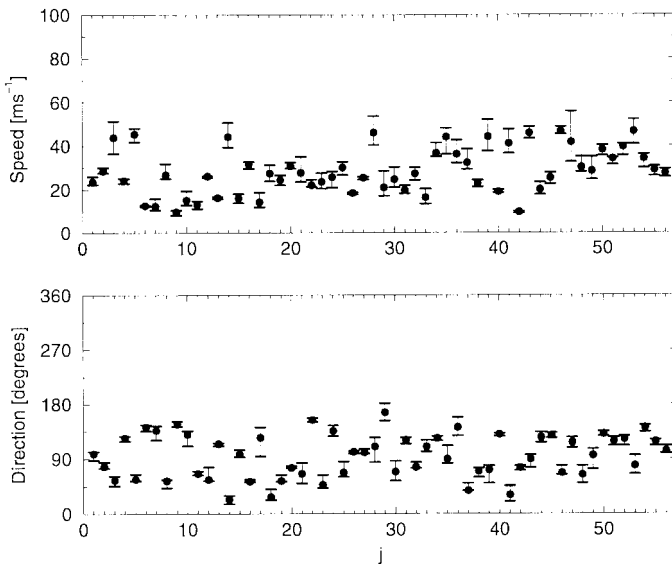

Fig. 13. Speed (top) and direction (bottom) of class 1 events for the fourth quarter of 1991. The horizontal axis corresponds to an index j numbering the class 1 events in order of extraction.
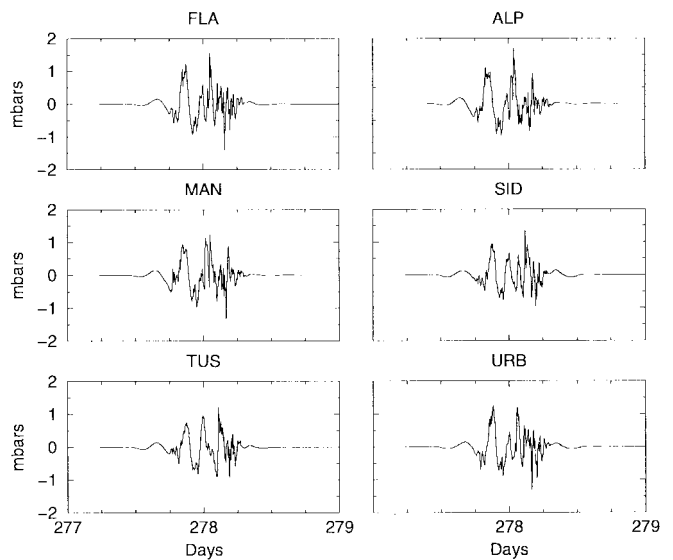

Fig. 14. Example of a bad event belonging to class 2i. The waveforms are significantly different in the various stations, and the cross-correlation coefficients are low.

amplitude of the event they really belong to, these fluctuations can result in false events with amplitude larger than the scale-dependent threshold $A(a)$. The fitting generally fails for these events because they are very different from one station to the other and the correlation coefficients are very poor.

iii) A third set of events is characterized by propagating wave packets with many cycles, short periods, and

small spatial wavelengths, like the one in Fig. 15. The centerband period of this wave is $T_s = 8$ min, and the number of oscillations is very large. This event, extremely significant, having a peak-to-peak value of almost 1 mbar, could not be fitted by a propagating plane wave because the presence of multiple maxima in the cross-correlation functions does not allow a unique determination of speed and direction. Moreover, the
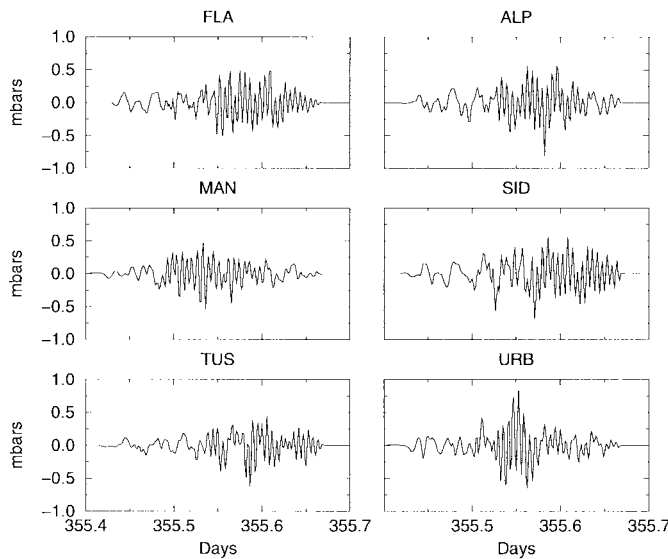
Fig. 15. Example of a well-defined event with a dominant frequency too large, with respect to the geometry of the barometer network, to be fitted with a propagating equivalent plane wave.

use of the cross-correlation functions for the determination of the delay times for these events should be avoided because low-frequency fluctuations, generally not coherent with the phase speed of the wave and different from station to station, lead to completely wrong results. Events of this kind can sometimes be analyzed by using additional information coming from other measurements, combined with analytical tools like the impedance relation, or by using a smaller-size measurement network.

It should be noted that the design of an automatic procedure for the discrimination of the three subclasses of events listed above is not a trivial task because the reasons for the failure of the fitting cannot be easily recognized.

V. CONCLUSIONS

We have described in detail an automatic algorithm to analyze the pressure records from a network of barographs located around Flatland, IL, and we have presented preliminary results for the last quarter of 1991 on the nature and frequency of occurrence of coherent disturbances detected by the network in the range from 30 min–6 h.

A powerful and selective adaptive-filtering procedure, based on the wavelet transform, localizes in time the events and provides a good reconstruction of their waveform at each station. Thus, the cross-correlations reach generally high values as a result of having minimized both the ambiguity in the determination of the integration domain and the effect of fluctuations that are extraneous to each event. A series of tests is discussed on the reconstruction of the signal at each station and on the allowed variability of the cross-correlation functions from station to station. As a result, class 1 events, satisfying all the requirements, including rather uniform speed and direction of propagation throughout the network and high cross-correlation coefficients (typically larger than 2/3), have been separated from the class 2 events, which fail some of

the requirements. Typical amplitude values range from 0.2 mbars at 10 min to several millibars at 2 h. The class 2 events have amplitudes above the chosen threshold and sometimes as large as for the class 1 events, but do not have high cross-correlation functions because they are either not uniform throughout the network or their characteristic horizontal scale is small compared with the size of the network.

The method has a number of limitations.

1) As expected, it does not work well when the signal is nearly monochromatic and lasts several periods of the disturbance. In these cases, the FFT method can be more efficient. However, the use of cross-correlation coefficients for the determination of speed and direction should be avoided when the spatial scale of the events is too small compared to the dimensions of the network.

2) It identifies as separate those events that in fact may have been generated by a single phenomenon: in parts (c) and (d) of Fig. 9, we see that numerous events have supports that overlap in time. This is the inevitable consequence of the fact that the method is automatic, and phenomena, such as a thunderstorm, go through various dynamical stages with distinct signatures in the pressure field and may generate disturbances with different characteristics. The frequency of occurrence of course would not be affected. Detailed studies on a case-by-case basis may make it possible to sort out the various components generated by a common source.

The analysis applied to the last quarter of 1991 shows that the class 1 events are present 18% of the time and, when class 2 events are added, the frequency of occurrence reaches 31%. The estimated speed for class 1 events is well within typical values of the jet streams, while the cone of dominant directions coincides with the general direction of the jet streams and jet streaks. These data confirm that the jet streams may be a source of gravity waves by shear instability [40] and can be a guiding mechanism for mesoscale waves as well, as discussed in [17], [50], and [52].

In general, the results of the climatology for the last quarter of 1991 presented in this paper indicate that mesoscale gravity waves are a common occurrence in the atmosphere. Since several case studies (see [17] and [49] and references therein) have demonstrated the ability of mesoscale waves to have a significant influence on the weather, this analysis confirms the need to gain a better understanding about their origin, the synoptic setting that favors their generation and propagation and about our ability to forecast them. The method presented in this paper appears to identify and extract them in a clear and effective way. To this end, the present study is being extended to an almost four-year period to obtain a more complete and accurate climatology and to investigate the seasonal dependence for speed, direction, amplitude, and especially frequency of occurrence of these disturbances.

REFERENCES

[1] Y. Brunet and S. Collineau, "Wavelet analysis of diurnal and nocturnal turbulence above a maize crop," in *Wavelets in Geophysics.* Boston, MA: Academic, 1994, pp. 129–150.

[2] F. Canavero and F. Einaudi, "Time and space variability of spectral estimates of atmospheric pressure," *J. Atmos. Sci.,* vol. 44, pp. 1589–1604, June 1987.

[3] D. R. Christie, "Long nonlinear waves in the lower atmosphere," *J. Atmos. Sci.,* vol. 46, pp. 1462–1491, June 1989.

[4] C. K. Chui, *An Introduction to Wavelets.* Boston, MA: Academic, 1992.

[5] C. Collineau and Y. Brunet, "Detection of coherent turbulent motions in a forest canopy. Part I: Wavelet analysis," *Boundary Layer Meteorol.,* vol. 65, pp. 357–379, 1993.

[6] J. M. Combes, A. Grossmann, and P. Tchamitchian, *Wavelets, Time-Frequency Methods, and Phase Space.* Berlin, Germany: Springer-Verlag, 1989.

[7] I. Daubechies, *Ten Lectures on Wavelets.* Philadelphia, PA: SIAM, 1992.

[8] A. Davis, A. Marshak, and W. Wiscombe, "Wavelet-based multifractal analysis of nonstationary and/or intermittent geophysical signals," in *Wavelets in Geophysics.* Boston, MA: Academic, 1994, pp. 249–298.

[9] N. Delprat, "Extraction of frequency modulation laws in sound synthesis," in *Wavelets and Applications.* Berlin, Germany: Springer-Verlag, 1992, pp. 3–11.

[10] N. Delprat, B. Escudié, P. Guillemain, R. Kronland-Martinet, P. Tchamitchian, and B. Torresani, "Asymptotic wavelet and Gabor analysis: Extraction of instantaneous frequencies," *IEEE Trans. Inform. Theory,* vol. 38, pp. 644–664, Mar. 1992.

[11] J. P. Djamdji and A. Bijaoui, "Disparity analysis: A wavelet transform approach," *IEEE Trans. Geosci. Remote Sensing,* vol. 33, pp. 67–76, Jan. 1995.

[12] F. Einaudi and J. J. Finnigan, "The interaction between an internal gravity wave and the planetary boundary layer. Part I: The linear analysis," *Q. J. R. Meteorol. Soc.,* vol. 107, pp. 793–806, Oct. 1981.

[13] F. Einaudi, A. J. Bedard, and J. J. Finnigan, "A climatology of gravity waves and other coherent disturbances at the boulder atmospheric observatory during Mar.–Apr. 1984," *J. Atmos. Sci.,* vol. 46, pp. 303–329, Feb. 1989.

[14] F. Einaudi, "Gravity waves in the troposphere," in *Diagnostic Tools in Atmospheric Physics,* G. Fiocco and G. Visconti, Eds. Oxford, U.K.: IOS Press, 1995, pp. 307–340.

[15] A. Erdelyi, *Higher Order Transcendental Functions, The Bateman Manuscript Project,* vol. 2. New York: McGraw-Hill, 1953.

[16] M. Farge, "Wavelet transforms and their applications to turbulence," *Annu. Rev. Fluid Mech.,* vol. 24, pp. 395–457, 1992.

[17] R. Ferretti, F. Einaudi, and L. W. Uccellini, "Wave disturbances associated with the Red River Valley severe weather outbreak of 10–11 Apr. 1979," *Meteorol. Atmos. Phys.,* vol. 39, pp. 132–168, 1988.

[18] N. Gamage and C. Hagelberg, "Detection and analysis of microfronts and associated coherent events using localized transforms," *J. Atmos. Sci.,* vol. 50, pp. 750–756, Mar. 1993.

[19] N. Gamage and W. Blumen, "Comparative analysis of low-level cold fronts: Wavelet, Fourier, and empirical orthogonal function decomposition," *Mon. Weather Rev.,* vol. 121, pp. 2867–2878, Oct. 1993.

[20] D. Gambis, "Wavelet transform analysis of the length of the day and the El-Niño/southern oscillation variations at intraseasonal and interannual time scales," *Ann. Geophysicæ,* vol. 10, pp. 429–437, 1992.

[21] W. Gao and B. L. Li, "Wavelet analysis of coherent structures at the atmosphere-forest interface," *J. Appl. Meteorol.,* vol. 32, pp. 1717–1725, Nov. 1993.

[22] S. M. Gollmer, Harshvardhan, R. F. Cahalan, and J. B. Snider, "Windowed and wavelet analysis of marine stratocumulus cloud inhomogeneity," *J. Atmos. Sci.,* vol. 52, pp. 3013–3030, Aug. 1995.

[23] A. Grossmann and J. Morlet, "Decomposition of hardy functions into square integrable wavelets of constant shape," *SIAM J. Math Anal.,* vol. 15, pp. 723–736, July 1984.

[24] A. Grossmann, R. Kronland-Martinet, and J. Morlet, "Reading and understanding the continuous wavelet transform," in *Wavelets, Time-Frequency Methods, and Phase Space.* Berlin, Germany: Springer-Verlag, 1989, pp. 1–20.

[25] P. Guillemain, R. Kronland-Martinet, and B. Martens, "Estimation of spectral lines with the help of the wavelet transform, applications in NMR spectroscopy," in *Wavelets and Applications.* Berlin, Germany: Springer-Verlag, 1992, pp. 38–60.

[26] C. R. Hagelberg and N. Gamage, "Applications of structure preserving wavelet decompositions to intermittent turbulence: A case study," in *Wavelets in Geophysics.* Boston, MA: Academic, 1994, pp. 45–80.

[27] T. Hauf, U. Finke, J. Neisser, G. Bull, and J.-G. Stagenberg, "A ground-based network for atmospheric pressure fluctuations," *J. Atmos. Ocean. Technol.,* vol. 13, pp. 1001–1023, Oct. 1996.

[28] T. J. Herron and I. Tolstoy, "Tracking jet stream winds from ground level pressure signals," *J. Atmos. Sci.,* vol. 26, pp. 266–269, 1969.

[29] J. F. Howell and L. Mahrt, "An adaptive decomposition: Application to turbulence," in *Wavelets in Geophysics.* Boston, MA: Academic, 1994, pp. 107–128.

[30] S. Kadambe and G. Faye Boudreaux-Bartels, "Application of the wavelet transform for pitch detection of speech signals," *IEEE Trans. Inform. Theory,* vol. 38, pp. 917–924, Mar. 1992.

[31] G. G. Katul, J. D. Albertson, C. R. Chu, and M. B. Parlange, "Intermittency in the atmospheric surface layer turbulence: The orthonormal wavelet representation," in *Wavelets in Geophysics.* Boston, MA: Academic, 1994, pp. 81–105.

[32] G. G. Katul and M. B. Parlange, "On the active role of temperature in surface-layer turbulence," *J. Atmos. Sci.,* vol. 51, pp. 2181–2195, Aug. 1994.

[33] P. Kumar and E. Foufoula-Georgiu, "A new look at rainfall fluctuations and scaling properties of spatial rainfall using orthogonal wavelets," *J. Appl. Meteorol.,* vol. 32, pp. 209–222, Feb. 1993.

[34] ——, "A multicomponent decomposition of spatial rainfall fields. 1: Segregation of large- and small-scale features using the wavelet transform," *Water Resource Res.,* vol. 29, pp. 2515–2532, Aug. 1993.

[35] ——, *Wavelets in Geophysics.* Boston, MA: Academic, 1994, pp. 1–43.

[36] K.-M. Lau and H. Weng, "Climate signal detection using wavelet transform: How to make a time series sing," *Bull. Amer. Meteorol. Soc.,* vol. 76, pp. 2391–2402, Dec. 1995.

[37] P. Liu, "Wavelet spectrum analysis of ocean wind waves," in *Wavelets in Geophysics.* Boston, MA: Academic, 1994, pp. 151–166.

[38] M. Mak, "Orthogonal wavelet analysis: Interannual variability in the sea surface temperature," *Bull. Amer. Meteorol. Soc.,* vol. 76, pp. 2179–2186, Nov. 1995.

[39] S. Mallat and S. Zhong, "Characterization of signals from multiscale edges," *IEEE Trans. Pattern Anal. Machine Intell.,* vol. 14, pp. 710–732, July 1992.

[40] G. Mastrantonio, F. Einaudi, D. Fua, and D. P. Lalas, "Generation of gravity waves by jet streams in the atmosphere," *J. Atmos. Sci.,* vol. 33, pp. 1730–1738, 1976.

[41] Y. Meyer, *Wavelets and Applications.* Berlin, Germany: Springer-Verlag, 1992.

[42] ——, *Wavelets and Operators.* Cambridge, U.K.: Cambridge Univ. Press, 1992.

[43] S. D. Meyers, B. G. Kelly, and J. J. O'Brien, "An introduction to wavelet analysis in oceanography and meteorology: With application to the dispersion of Yanai waves," *Mon. Weather Rev.,* vol. 121, pp. 2858–2866, Oct. 1993.

[44] S. D. Meyers and J. J. O'Brien, "Spatial and temporal 26-day SST variations in the equatorial Indian Ocean using wavelet analysis," *Geophys. Res. Lett.,* vol. 21, pp. 777–780, May 1994.

[45] J. Morlet, G. Arens, E. Fourgeau, and D. Giard, "Wave propagation and sampling theory–Part II: Sampling theory and complex waves", *Geophysics,* vol. 47, pp. 222–236, Feb. 1982.

[46] A. Papoulis, *Probability, Random Variables, and Stochastic Processes.* New York: McGraw-Hill, 1965.

[47] W. H. Press, B. P. Flannery, S. A. Teukolsky, and W. T. Vetterling, *Numerical Recipes.* Cambridge, U.K.: Cambridge Univ. Press, 1984.

[48] K. Sato and M. Yamada, "Vertical structure of atmospheric gravity waves revealed by the wavelet analysis," *J. Geophys. Res.,* vol. 99, pp. 20623–20631, Oct. 1994.

[49] R. S. Schneider, "Large-amplitude mesoscale wave disturbances within the intense midwest extratropical cyclone of 15 Dec. 1987," *Weather Forecasting,* vol. 5, pp. 533–558, 1990.

[50] J. G. Stobie, F. Einaudi, and L. W. Uccellini, "A case study of gravity waves-convective storms interactions: 9 May 1979," *J. Atmos. Sci.,* vol. 40, pp. 2804–2830, 1983.

[51] L. W. Uccellini, "A case study of apparent gravity wave initiation of severe convective storms," *Mon. Weather Rev.,* vol. 103, pp. 497–513, 1975.

[52] L. W. Uccellini and S. E. Koch, "The synoptic setting and possible energy sources for mesoscale wave disturbances," *Mon. Weather Rev.,* vol. 115, pp. 721–729, 1987.

[53] H. Weng and K.-M. Lau, "Wavelets, period doubling, and time-frequency localization with application to organization of convection over the tropical western Pacific," *J. Atmos. Sci.,* vol. 51, pp. 2523–2541, Sept. 1994.

[54] S. A. Werness, S. C. Wei, and R. Carpinella, "Experiments with wavelets for compression of SAR data," *IEEE Trans. Geosci. Remote Sensing,* vol. 32, pp. 197–201, Jan. 1994.

Stefano Grivet-Talocia received the electronic engineering degree from Politecnico of Turin, Turin, Italy, in 1994.

From 1994 to 1996, he was at Goddard Space Flight Center, Greenbelt, MD, where he carried out research in the Laboratory for Atmospheres. His work concentrated on the application of fractal geometry and wavelet transform to the analysis and processing of geophysical time series. In particular, he worked on atmospheric pressure data to detect and study gravity wave events. He has been a Researcher with the Electronics Department, Politecnico of Turin, since 1996. His primary research interests are fractals, wavelets, and their application to the field of electromagnetic compatibility, specifically, signal processing and adaptive solution of PDE's.

Franco Einaudi received the B.S. degree from Politecnico of Turin, Turin, Italy, and the M.S. and Ph.D. degrees from Cornell University, Ithaca, NY.

From 1969 to 1979, he was with the Cooperative Institute for Environmental Sciences (CIRES), University of Colorado and NOAA, both located in Boulder, CO. He was a Professor of Geophysical Sciences at Georgia Institute of Technology, Atlanta, from 1979 to 1987. He has been the Chief of the Laboratory for the Atmospheres, Goddard Space Flight Center, Greenbelt, MD, since 1990. His primary research interests are gravity wave generation and propagation, interaction with turbulence, and convective processes.